TU
WIEN

TECHNISCHE UNIVERSITÄT WIEN

DIPLOMARBEIT

Resistivity and Hall effect measurements in disordered YBCO films

ausgeführt am

Atominstitut

unter der Anleitung von

Privatdoz. Dipl.-Ing. Dr.techn. Michael Eisterer
Projektass. Dipl.-Ing. Raphael Unterrainer

durch

Alexander Bodenseher

01226485

März 2022

Abstract

The main goal of this thesis was to measure the resistive and Hall effect properties of $YBa_2Cu_3O_{7-\delta}$ thin films deposited on a magnesium oxide substrate and the behavior after subsequent thermal treatment and in preparation for irradiation with neutrons in the TRIGA Mark-II reactor of the Atominstitut.

The sample layout was designed, and the samples were manufactured by the Leibniz Institute for Solid State and Materials Research in Dresden. A new sample holder matching the sample layout was designed and manufactured.

Since the contact resistance of YBCO is very high, the contact pads for a 4-wire sensing configuration were sputtered with $1\,\mu m$ of silver. The samples were measured in the $17\,T$ cryostat with a current of $10\,mA$ at fields up to $\pm 15\,T$. During the measurement, the temperature was ramped from up to $250\,K$ down to below T_c. Afterwards, the samples were thermally treated in a tube furnace in a pure oxygen atmosphere at ambient pressure, followed by another measurement. These steps were repeated several times at various temperatures and durations until T_c and the normal state resistivity stabilized. This was done to establish a baseline measurement before neutron irradiation.

T_c and ρ stabilized at annealing temperatures between $350\,°C$ and $400\,°C$. Temperatures above $600\,°C$ destroyed two samples. A decrease in charge carrier density between pristine and thermally treated samples was observed.

Kurzfassung

Im Rahmen dieser Arbeit wurde das Verhalten des spezifischen Widerstands und der Hallkonstante von auf Magnesiumoxid deponierten $YBa_2Cu_3O_{7-\delta}$ Dünnschichtfilmen vor und nach thermischer Behandlung untersucht. Die Proben wurden für die Bestrahlung mit Neutronen im TRIGA Mark-II Reaktor des Atominstituts vorbereitet.

Die Proben wurden im Leibniz-Institut für Festkörper- und Werkstoffforschung Dresden präpariert. Ein neuer Probenhalter, abgestimmt auf das neue Probendesign wurde geplant und gefertigt.

Da der Übergangswiderstand von YBCO sehr hoch ist, wurden auf die Kontaktstellen 1 μm dicke Silberkontakte gesputtert. Die Proben wurden im 17 T Kryostaten bei Feldern bis zu ±15 T gemessen. Der Widerstand der Probe wurde mittels Vierleitermessung bei einem angelegten Strom von 10 mA gemessen, während die Temperatur beginnend von 250 K bis unter die kritische Temperatur schrittweise reduziert wurde. Danach wurden die Proben in reiner Sauerstoffatmosphäre bei Umgebungsdruck thermisch behandelt. Daraufhin wurden die Proben erneut gemessen. Diese Schritte wurden mehrmals bei verschiedenen Temperaturen und Behandlungszeiten wiederholt, bis sich T_c und der spezifische Widerstand stabilisierten und eine Grundlage für die Messung nach der Bestrahlung liefern.

T_c und ρ stabilisierten sich bei Temperaturen zwischen 350 °C und 400 °C. Zwei Proben wurden durch Temperaturen über 600 °C zerstört. Eine Reduktion der Ladungsträgerdichte zwischen unbehandelten und behandelten Proben konnte beobachtet werden.

Contents

1 Introduction

For our necessary transition to sustainable future we have to develop new ways of generating electricity. One of those ways is nuclear fusion, harnessing the power of the sun on earth. Fusion reactions can only happen under the most extreme circumstances, therefore, for one approach, we have to confine a plasma—several hundred million degrees hot—consisting of fusion fuel inside a reactor. This confinement is provided by magnetic fields, which are powered by superconducting coils.

The fusion reaction creates neutron radiation which damages equipment, and turns the vicinity of the reactor to one of the most demanding industrial environments currently known. This has significant implications on cost and durability of the employed magnets. [1]

One candidate for those superconducting magnets are high temperature superconductors and the goal of this work is to investigate their behavior under neutron radiation and potential restoration by thermal treatment in an oxygen atmosphere. Previous work has concentrated on coated conductors [1, 2], which are tapes consisting of a superconducting core and various buffer and stabilizing layers, with the outermost being films of silver or copper, whereas the samples used in this thesis are YBCO deposited via pulsed laser deposition on a substrate of magnesium oxide, which have been manufactured by the Functional Oxide Layers and Superconductors group at IFW Dresden.

The bare YBCO enables the study of its properties, without the influence of impurities caused by the buffer layers of coated conductors. Magnesium oxide has been chosen as substrate material, since it still can be handled safely after

neutron activation.

The layout of the samples has been chosen to facilitate resistive and Hall effect measurements. Since these samples have no conducting layer around them contacting them reliably is challenging. Over the course of this thesis a new sample holder has been designed and several methods of creating a reliable contact between the sample and the measurement setup have been investigated.

Following the development of an acceptable procedure, resistive and Hall voltages have been measured, and the samples have been thermally treated several times to stabilize the superconducting properties, i.e. T_c and the normal state resistivity in order to isolate the effects of the neutron radiation on the superconducting performance of the samples and their development after subsequent thermal treatment in oxygen. The behavior of the samples and the changes after each subsequent thermal treatment step are presented and discussed in chapter 4.

2 Fundamental concepts

2.1 Superconductivity

The electrical resistance of metals is governed by scattering of electrons by phonons, electron-electron interaction and scattering by lattice defects. Since lattice defects are independent of the temperature, one would expect a residual resistance close to absolute zero. Furthermore, the magnetic susceptibility of metals should not show any temperature dependence, because the theories of Landau diamagnetism and Pauli paramagnetism are temperature independent.

Investigations of the low temperature behavior of metals led to the discovery of the superconducting state by Heike Kamerlingh Onnes [6]. Below the material dependent critical temperature T_c, the electrical resistivity disappears completely. Another essential property of superconductors, the expulsion of applied external fields (i.e. perfect diamagnetism) was discovered by Meißner and Ochsenfeld [7]. This expulsion cannot be explained by perfect conductivity, which would either exclude magnetic fields from entering the superconductor or trap magnetic flux inside it. This makes the transition to and from superconductivity a reversible process and superconductivity a thermodynamic state.

The resulting thermodynamic state implies, that superconductivity will be destroyed by a critical magnetic field, H_c, since the superconductor cannot do an infinite amount of work expelling external fields.

The difference between the Gibbs free energy in the normal and the super-

3

conducting state is

$$\mathfrak{g}_n(T) - \mathfrak{g}_s(T) = \frac{\mu_0 H_c^2(T)}{2} \, .$$ (2.1)

This expression is called the condensation energy density and defines the critical field H_c. Its temperature dependence can be approximated by the following empirically found parabolic law

$$H_c(T) \approx H_c(0) \left[1 - \left(\frac{T}{T_c} \right)^2 \right] \, .$$ (2.2)

2.1.1 London Equations

The London equations are an attempt to describe the perfect conductivity and ideal diamagnetism within the framework of classical electrodynamics [8]. They describe the perfect conductivity of a superconductor and provide an explanation of the Meißner-Ochsenfeld-Effect.

The first equation replaces Ohms law with:

$$\frac{\partial(\Lambda \mathbf{J}_s)}{\partial t} = \mathbf{E} \, .$$ (2.3)

Where $\mathbf{J}_s$ is the supercurrent density, $\Lambda = \frac{m_s}{n_s q_s^2}$, also called the London parameter and m_s and n_s are the mass and density per unit volume of the superconducting electrons.

The second London equation connects the current density with the magnetic flux within the superconductor

$$\nabla \times (\Lambda \mathbf{J}_s) + \mathbf{b} = 0 \, ,$$ (2.4)

where $\mathbf{b}$ is the microscopic magnetic flux density.

Using Maxwells equations the second London equation can be rewritten as

$$\Delta \mathbf{b} = \frac{1}{\lambda_{\mathrm{L}}^2} \mathbf{b} \tag{2.5}$$

$$\lambda_{\mathrm{L}} = \sqrt{\frac{\Lambda}{\mu_0}} = \sqrt{\frac{m_s}{\mu_0 n_s q_s^2}} \ . \tag{2.6}$$

Equation (2.5) implies, that the magnetic field is exponentially screened from the interior of the superconductor with λ_{L} defined as the London penetration depth.

However, experiments show, that superconducting penetration depths λ are always larger than λ_{L} as predicted by the London equations. A quantitative treatment of superconducting penetration depths requires a nonlocal generalization of the London equation, which was derived by Pippard [9].

2.1.2 Ginzburg-Landau Equations

The Ginzburg-Landau Theory is based on Landau's theory of phase transitions. A pseudowavefunction $\psi(\mathbf{r})$ is introduced as complex order parameter with $|\psi(\mathbf{r})|^2$ representing the local density of superconducting electrons. The order parameter has to be zero above the superconducting transition temperature and finite below.

Under the assumption that the order parameter ψ is small and varies slowly in space the free energy density can be expanded in a series of the form

$$f_s(\mathbf{r}) = f_n(\mathbf{r}) + \alpha |\psi|^2 + \frac{\beta}{2} |\psi|^4 + \frac{1}{2\mu_0} (\mathbf{B}_{\mathrm{ext}} - \mathbf{b})^2$$
$$+ \frac{1}{2m_s} |(-i\hbar\nabla - q_s\mathbf{A})\psi|^2 + \dots \ . \tag{2.7}$$

By solving the variational problem with respect to the order parameter and

the free energy one can derive the Ginzburg-Landau equations

$$\alpha\psi + \beta|\psi|^2\psi + \frac{1}{2m_s}\left(\frac{\hbar}{i}\nabla - q_s\mathbf{A}\right)^2\psi = 0 \tag{2.8}$$

$$\mathbf{J_s} = \frac{q_s\hbar}{2m_s i}\left(\psi^*\nabla\psi - \psi\nabla\psi^*\right) - \frac{q_s^2}{m_s}|\psi|^2\mathbf{A}. \tag{2.9}$$

The first equation—apart from the nonlinear term—has the form of Schröding-er's equation, with energy eigenvalue $-\alpha$ while the nonlinear term acts like a repulsive potential. The second equation provides the supercurrent and has the usual form of a quantum probability current equation.

Furthermore, two characteristic lengths can be derived from the Ginzburg-Landau equations. With the assumption of constant density of superconducting electrons, the London equations and the magnetic penetration depth can be derived. This penetration depth delimits the scale on which the magnetic flux density can change.

Rewriting the first Ginzburg-Landau equation with $\Psi = \frac{\psi}{\psi_0}$ and $|\psi_0|^2 = -\frac{\alpha}{\beta}$ yields the following:

$$\frac{\hbar^2}{2m_s\alpha}\left(-i\nabla - \frac{q_s}{\hbar}\mathbf{A}\right)^2\Psi + \Psi - |\Psi|^2\Psi = 0. \tag{2.10}$$

$\frac{\hbar^2}{2m_s\alpha}\nabla^2\Psi$ is a dimensionless quantity, thus $\xi_{\mathrm{GL}} = \sqrt{\frac{\hbar^2}{2m_s\alpha}}$ can be interpreted as the second characteristic length, the Ginzburg-Landau coherence length. It describes the scale of the local variation of the order parameter. The ratio between these two lengths is the dimensionless Ginzburg-Landau parameter κ.

Gor'kov derived the Ginzburg-Landau theory as a limiting case of the micro-scopic BCS theory[1] and Abrikosov solved the Ginzburg-Landau equation for the mixed state and predicted the existence of flux lines [10, 11].
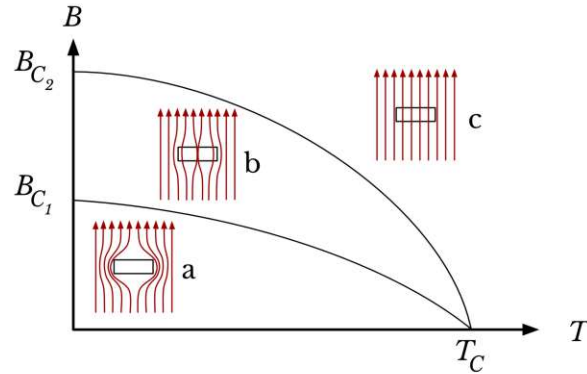
---

[1]See section 2.1.4

Figure 2.1: Phase diagram of a type-II superconductor. (a) Below $B_{C_1} = \mu_0 H_{C_1}$ the superconductor remains in the Meißner phase. (b) Above B_{C_1} it enters the Shubnikov phase with flux vortices penetrating the interior of the superconductor. (c) Above B_{C_2} and T_C the superconductor transitions into the normal state with magnetic flux freely penetrating it. [12]

2.1.3 Type-I and Type-II Superconductors

Superconductors can be classified into type-I and type-II superconductors. The characteristic properties of both types can be described using the Ginzburg-Landau parameter

$$\kappa = \frac{\lambda_{\mathrm{GL}}}{\xi_{\mathrm{GL}}} \begin{cases} < \frac{1}{\sqrt{2}} & \text{type-I superconductor} \\ > \frac{1}{\sqrt{2}} & \text{type-II superconductor .} \end{cases} \tag{2.11}$$

This relation determines the behavior of the superconductor in an external magnetic field. The Ginzburg-Landau parameter is related to the surface energy at the interphase of the superconducting and normal phase. For $\kappa < \frac{1}{\sqrt{2}}$ the surface energy at H_c is positive and the energetically most favorable state is the state with the least amount of superconducting and normal state interphase boundary. Thus, the superconductor remains in the Meißner state until the external field exceeds the critical field H_c. Most superconducting elements

are type-I superconductors. However, T_c, H_c and J_c are very low for type-I superconductors, which make them impractical for technical applications.

For $\kappa > \frac{1}{\sqrt{2}}$ the surface energy at H_c is negative, thus it becomes energetically preferential for the superconductor to lower its overall energy level, by letting quantized magnetic flux lines penetrate the interior. This happens above the lower critical field $B_{c_1} = \mu_0 H_{c_1}$ (see figure 2.1).

Flux lines carry a quantized flux quantum $\Phi_0 = \frac{h}{2e}$ generated by current vortices surrounding the core. A type-II superconductor remains in the superconducting state up to an upper critical field H_{c_2} which can be in the range of $>100\,\mathrm{T}$.

Flux pinning

Flux lines inside a superconductor repel each other and inside a perfectly clean superconductor they form a hexagonal lattice with the distance

$$a = \sqrt{\frac{2\phi_0}{\sqrt{3}B}} \tag{2.12}$$

separating them. Any applied current causes the flux lines to move, due to the Lorentz force between flux line and current, with the Lorentz force density being $\mathbf{f_L} = \mathbf{J} \times \mathbf{B}$. As a result the flux lines move transverse to the current with the velocity $\mathbf{v_L}$ and induce an electrical field $\mathbf{E} = \mathbf{B} \times \mathbf{v_L}$, which acts like a resistive voltage and causes current dissipation. Therefore, a clean type-II superconductor with an external field above H_{c_1} and below H_{c_2} is unable to sustain persistent current.

This behavior is obviously impractical for technical applications. However, a spatial inhomogeneity of the material, i.e. crystal defect, impurities or grain boundaries can be an energetically favorable place for the flux line, which in result causes it to *pin* in place. It remains in place as long as the *pinning force* remains smaller than the Lorentz force caused by the current. The pinning

force is also weakened at high temperature by thermal fluctuations within the material. The most effective defects must be on the scale of ξ ($\sim 1\,\mathrm{nm}$ for YBCO).

2.1.4 BCS Theory

Cooper demonstrated, that an arbitrary small attractive potential creates bound electron pairs [13]. In conventional superconductors, this attractive force is mediated by phonons, however, in more exotic superconductors other virtual exchange bosons may also be responsible for the creation of Cooper pairs.

Consider two electrons added to the Fermi sea at $T = 0$. These electrons possess a wave function of the sort

$$\psi(\mathbf{r_1}, \mathbf{r_2}) = \sum_{\mathbf{k}} a_{\mathbf{k}} e^{i\mathbf{k}\mathbf{r_1}} e^{-i\mathbf{k}\mathbf{r_2}} . \tag{2.13}$$

Calculating the energy of this wave function yields

$$E \simeq 2E_{\mathrm{F}} - 2\hbar\omega_{\mathrm{D}} e^{-\frac{4}{D(E_{\mathrm{F}})V_0}} . \tag{2.14}$$

This represents a bound state with an energy below the Fermi energy E_{F} made up of electrons with a kinetic energy larger than E_{F}. Using the uncertainty principle the size of a Cooper pair can be estimated in the range of $10\,\mathrm{nm}$ to $100\,\mathrm{nm}$. Since the electron density in metals is around $10^{22}\,\mathrm{cm^{-3}}$ to $10^{23}\,\mathrm{cm^{-3}}$, the Cooper pairs are highly overlapping and thus condense into a macroscopic quantum state.

The model shown above was generalized to the whole electron system with the derivation of the BCS wave function by Bardeen, Cooper and Schrieffer. The complete derivation shall be deferred to [3, 4, 14, 15], however one significant

result is the relation between the critical temperature and the Debye frequency.

$$k_{\mathrm{B}}T_c = 1.13 \ \omega_{\mathrm{D}} e^{-\frac{2}{D(E_{\mathrm{F}})V_0}} \propto \omega_{\mathrm{D}} \propto M^{-\frac{1}{2}} \ . \tag{2.15}$$

The phonon frequency for different isotopes of the same element is proportional to the isotope mass $M^{-\frac{1}{2}}$. This relation—the isotope effect—is in agreement with experimental evidence and important prediction by the BCS-Theory.

2.1.5 High Temperature Superconductors

Most high temperature superconductors are either copper based ceramics—i.e. *cuprates* or iron based compounds. The first high temperature superconductor was discovered in 1986 by Bednorz and Müller $Ba_x La_{5-x} Cu_5 O_{5(3-y)}$ [16] and soon after $YBa_2 Cu_3 O_{7-\delta}$ with an T_c of 93 K, which is above the boiling point of liquid nitrogen, was discovered [17].

All known high temperature superconductors are type-II superconductors, therefore understanding and manipulating the mixed phase is of utmost importance for achieving high currents and magnetic fields in technical applications. No consensus has been reached on the mechanism driving high temperature superconductivity, with one of the reasons being the complex crystal structures of the materials in question.

There is evidence, that the key to understanding the mechanism of high temperature superconductivity lies in the behavior of the HTS above T_c [19]. In the default configuration most high temperature superconductors are Mott insulators[2]. Doping the material with either additional charges, either electrons or holes, turns it into a regular conductor above T_c and a superconductor below T_c (see figure 2.2). Maximum T_c is observed at *optimal* doping.

---

[2]In a Mott insulator the energy band is half filled, but due to the strong Coulomb repulsion between individual electrons the material remains in an insulating antiferromagnetic state.
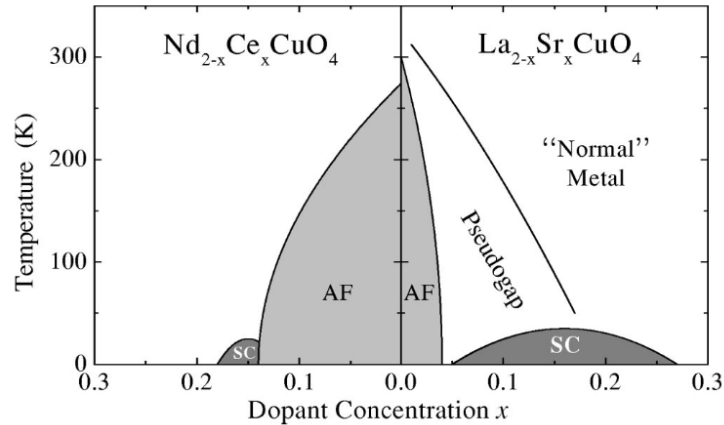
Figure 2.2: Phase diagram showing electron doping on the left, hole doping on the right and the doping dependent antiferromagnetic phase, pseudogap and superconducting state. From [18].

Scaling relations

Several relations correlating physical quantities in high temperature and conventional superconductors have been discovered [20]. The first one is the Uemura relation, which states $T_c \propto \rho_s$, with ρ_s being the superfluid density. It was first discovered for underdoped cuprates, but it also holds true for overdoped cuprates [21, 22].

An extension—Homes' law states $\sigma_{\mathrm{dc}} T_c \propto \rho_s$, with σ_{dc} being the normal state DC conductivity close to T_c. This relation holds true for under and overdoped high temperature superconductor and also for conventional superconductors [23]. The connection between the superfluid density and T_c cannot be explained with our current understanding of the theory of superconductivity.

Cuprates

Cuprates are a family of high temperature superconductors consisting of copper oxide layers stacked alongside the c-axis and separated by layers of metal oxides.
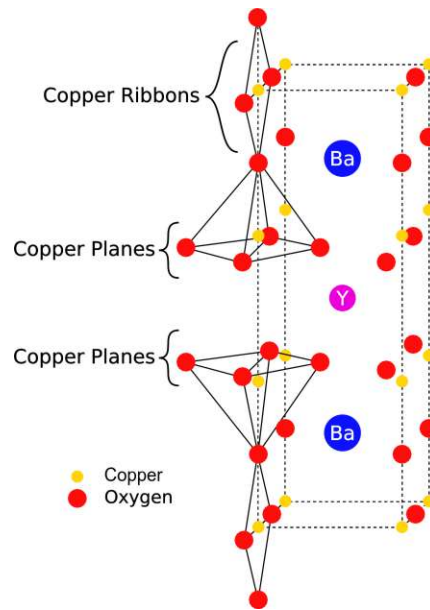
Figure 2.3: YBCO crystal structure. From [25]

The undoped "parent" compounds are Mott isolators with an antiferromagnetic order. Doping cuprates with additional holes or electrons provides additional charges for the copper oxide layers, which are believed to be the root cause for superconductivity.

An important class of cuprates are rare earth barium copper oxides, known as REBCO, with the most prominent being Yttrium Barium Copper Oxide (YBCO). As all cuprates $YBa_2Cu_3O_{7-\delta}$ with $\delta = 1$ is a Mott insulator. In this configuration the copper ribbons are fully filled, at $\delta = 0$ they are empty. The maximum transition temperature of around 90 K to 92 K has been reported at around $\delta \sim 0.07$ [24].
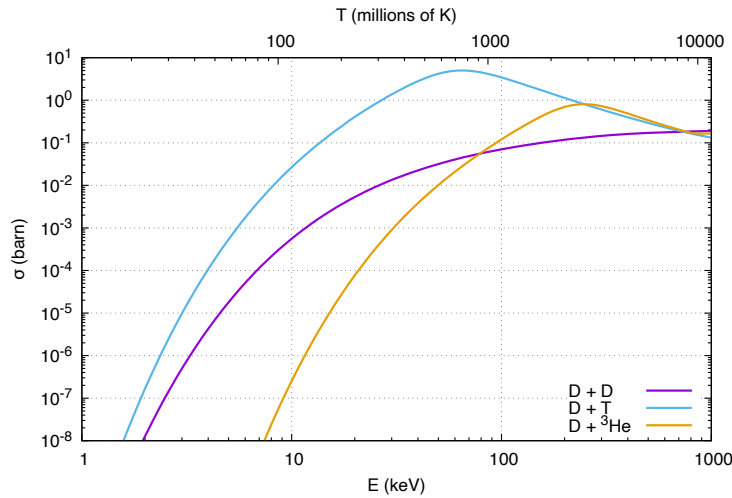
Figure 2.4: Cross sections of nuclear fusion reactions. The D-T Fusion rate peaks at around 800 million K with the highest cross section, compared to the other reactions. Calculated from IAEA Evaluated Nuclear Data File data [26].

2.2 Nuclear fusion

Two colliding atoms or subatomic particles (neutrons or protons) can fuse together, forming a heavier nucleus, granted they have sufficient energy to overcome the Coulomb barrier. Depending on the reaction, the difference in mass between the incoming and outgoing particles will be released as energy. Fusion reactions have been powering the sun for over five billion years and are a promising solution to our necessary transformation to clean and sustainable energy.

The most promising reaction for artificial fusion is

$$\mathrm{^{2}_{1}H} + \mathrm{^{3}_{1}H} \longrightarrow \mathrm{^{4}_{2}He}(3.5\,\mathrm{MeV}) + \mathrm{n}(14.1\,\mathrm{MeV}),$$
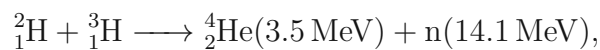
which nets 17.6 MeV of energy per fusion reaction.

As stated above, the reactants have to be heated sufficiently to overcome the

electrostatic forces between particles with a positive charge. To facilitate this, there have been several proposed and tested approaches. The most relevant one for this thesis is magnetic confinement fusion (MCF), in which the fusion fuel is confined as a plasma by strong magnetic fields. The most intensively studied type of MCF fusion reactor is the Tokamak reactor, which confines the plasma in the shape of a torus.

Estimating the fusion power density gives $P_{\text{Fusion}} \propto \beta^2 B^4$ [2]. This means, the power output of a fusion reactor is extremely dependent on the highest possible fields. Therefore, using high temperature superconductor with their high critical fields is advantageous for constructing smaller and more efficient nuclear fusion reactors.

# 3 Experimental methods, sample preparation and measurements

3.1 Samples

The samples are YBCO grown from pulsed laser deposition (PLD) on a MgO substrate, prepared by the Functional Oxide Layers and Superconductors group at IFW Dresden. The samples are a layer $1\,\mu m$ YBCO on $1\,mm$ magnesium oxide. Two batches of samples were produced with the samples of the first batch being designated as IS70, IS71, IS74 and the second batch IS246, IS247, IS248, IS249. Since magnesium oxide is rather brittle the samples have to be handled delicately. Nonetheless, samples IS70, IS71 were destroyed during insertion into and assembly of the sample holder.

The layout has been chosen to measure resistivity and Hall voltage in a 4 wire configuration with the rectangular bars on the top and bottom, shown in figure 3.1a, being the current contacts, and the circular pads the voltage contacts.

Due to manufacturing imprecision the pristine samples had bridges of YBCO running down the left and right side. These bridges distort the measured voltage across the circular measurement pads, therefore the edges of the central bridge and circular pads where masked with nail polish and the edges were carefully etched with hydrochloric acid.
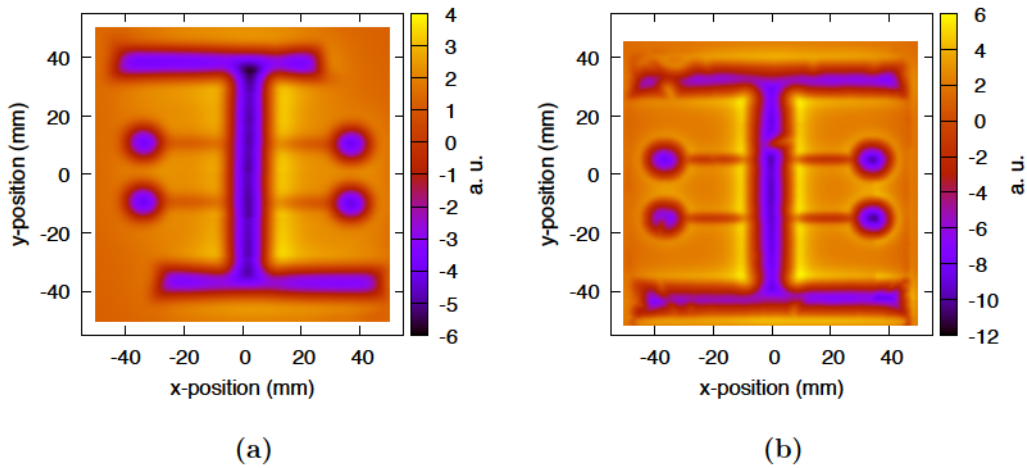
The samples have been examined in a Hall scanner [27, 28] in liquid nitrogen
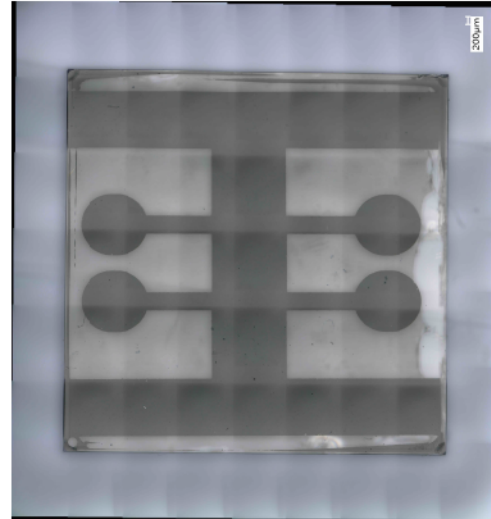
(a)   (b)

Figure 3.1: (a) The layout of the sample with dimensions in mm with the four
contact pads for measuring resistivity and Hall voltage. (b) Microscope
image of pristine sample IS74.

(a)   (b)

Figure 3.2: (a) Hall scan of sample IS246 after etching the corners and before
sputtering. (b) Scan of pristine IS247. Clearly visible is an imperfection
on the central bridge.

at 77 K. Sample IS247 showed damage in the central bridge (see figure 3.2b), therefore it was not used for Hall effect measurements. The samples exhibited no deterioration after sputtering. Figure 3.3 shows IS74 after several rounds of depositing gold, etching, sputtering silver and annealing. There is significant degradation of the YBCO visible, therefore this sample can be considered destroyed.
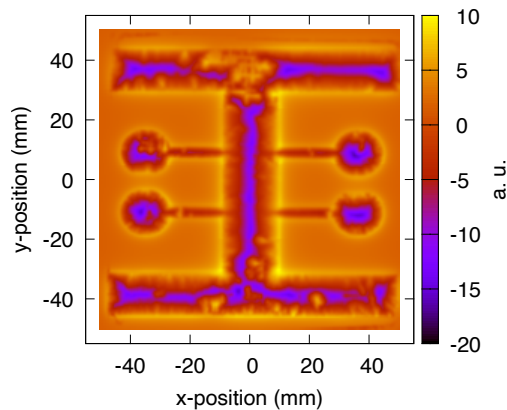

Figure 3.3: Hall scan of IS74 after depositing gold, measuring, etching, sputtering, annealing. The degradation of the YBCO layer is visible.

3.2 Development of low resistance contacts

The challenge of establishing a reliable electrical connection between YBCO and the measurement setup has been previously reported [29, 30] and has once again been confirmed over the course of this thesis. In previous experiments with coated conductors the connection has been made with spring-loaded pins on the copper or silver coating. The samples in this thesis, however, are bare YBCO, which is a non-ductile ceramic consisting of large high contact resistance crystal grains. Therefore, the semi-spherical tips of the spring-loaded pins cannot establish a reliable connection.
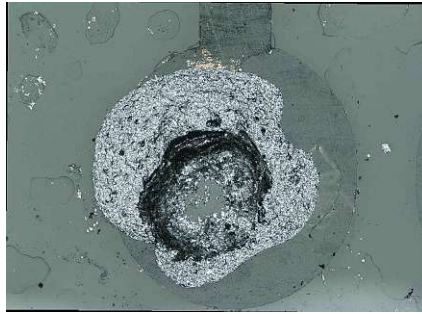
Figure 3.4: Contact pad on IS74 with a layer of conducting paint, after measurement.

Since the samples are going to be irradiated, it is necessary to work as fast as possible to limit exposure to radiation. Therefore, samples and sample holder have to be disassembled and assembled in a swift and straightforward way. This is the principal motivation for choosing the method of creating the electrical bond between the sample and the rest of the measurement system.

Several methods of improving the electrical connection have been investigated and will be described in the following sections.

Conductive silver paint

The first one was conductive silver paint, which has led to acceptable results in earlier experiments.

However, conductive silver paint has shown to be inadequate. It is difficult to apply it reliably to the six spots, where the spring-loaded pins connect to the sample. Even if a connection is made, the contact resistance is rather high (in the range of $200\,\Omega$ to $500\,\Omega$) and there is still a high chance, that the contact will open upon insertion of the sample holder into the $17\,\mathrm{T}$ cryostat. Figure 3.4 shows one circular contact pad painted with conductive silver paint after a full measurement cycle. One can clearly see that the silver paint has been scratched off by the spring-loaded pins. Therefore, conductive silver paint has been ruled out.

Gold physical vapor deposition

The next explored method was physical vapor deposition. Assistance was provided by the Functional and Magnetic Materials Group of the Institute of Solid State Physics. The sample was masked with a piece of FR-2 with holes drilled in the same positions as the current pins and circular contact pads. 1.5 g of Gold were heated in a vacuum inside the physical vapor deposition machine and then deposited on the sample. The initial contact resistance measurements were promising, but the adhesion of the gold layer was insufficient, as seen in 3.5a.

Due to the aforementioned problem with adhesion, the fact, that gold becomes activated after the exposure of neutron radiation, which would mean small pieces of torn off gold contaminating the measurement setup, the expense of coating even one sample and that it cannot be done in house, physical vapor deposition was ruled out.

3.2.1 Sputter deposition

Sputtering is a technique to deposit a thin film of material on a substrate. In this process ions are accelerated onto a target, with the subsequent collision causing some target atoms to be ejected. These ejected atoms fly on a ballistic trajectory until they reach the substrate, where they bind to the surface.

Extensive work on finding the ideal sputter parameters and settings for the sputtering machine of the institute and describing the whole apparatus and process has been done in [30]. The sputter parameters taken from the aforementioned work have been used throughout all sputter depositions and are listed in table 3.1. A sputter mask was machined out of FR-2 (see figure 3.7), into which the sample was inserted while sputtering. Right after sputtering the silver layer exhibits the same problems as the gold one, with it being scraped off by the spring-loaded pins. However, by thermally treating it in a pure oxygen atmosphere at a temperature above 200 °C, the layer becomes much
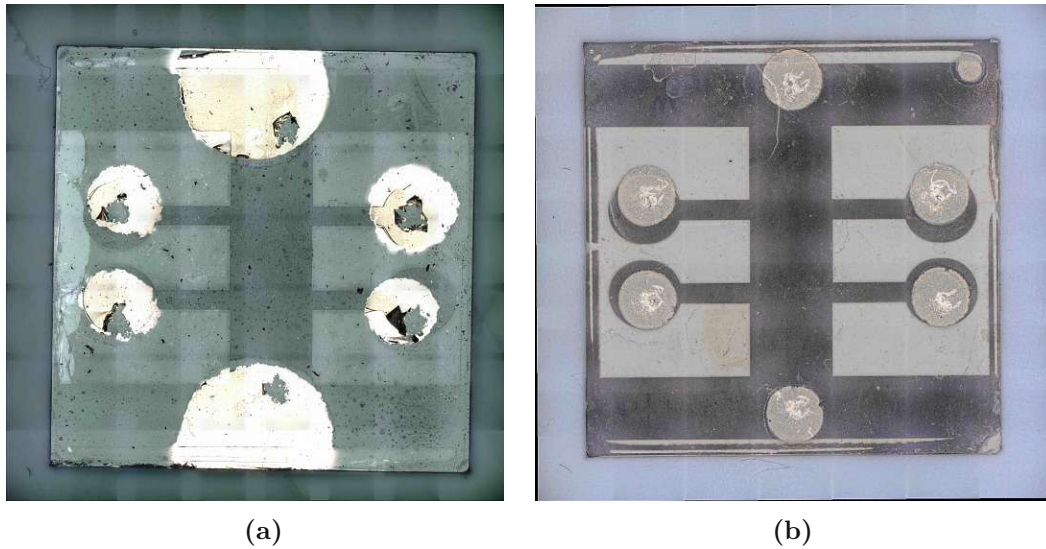
(a)   **(b)**

Figure 3.5: (a) IS74 coated with gold, after five days of measurement. (b) IS249 showing sputtered silver layer after annealing and measuring. The surface has been scratched by the spring-loaded pins, but no tearing is visible.

power setting	100 W
discharge voltage	430 V
argon pressure	$1.3 \cdot 10^{-3}$ mbar
target substrate distance	80 mm
sputtering time	10 min
sputtering gas	Argon
layer thickness	1 µm
sputtering target	¼″ 99.99 % silver

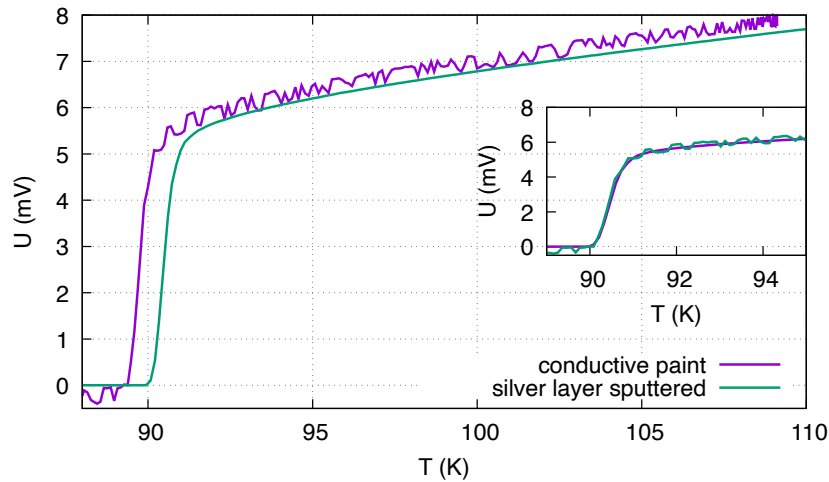**Table 3.1:** Sputter parameters used for all sputtered samples.

Figure 3.6: IS248 measured with conductive silver paint and after sputtering. The insert shows the same measurement with the curve referring to the sample before sputtering shifted by 0.7 K

more robust and durable.

Figure 3.6 shows the influence of conductive paint and sputtering on the measurements. Conductive paint results in high contact resistance and therefore in noisier measurements and due to ohmic heating of the sample in a decreased measured T_c. Shifting the measurement with conductive paint by 0.7 K shows, that the superconducting transition did not change. This indicates, that the initial sputtering does not change the properties of the samples.

Damaged silver layers have been removed with a solution of hydrogen peroxide and ammonia, with a ration of 2:1:1 of deionized water, 30 % hydrogen peroxide, and 25 % of ammonia.

3.3 Thermal treatment

The samples were heat treated in a tube furnace to stabilize the superconducting properties, establish baseline measurements and prepare the samples for neutron
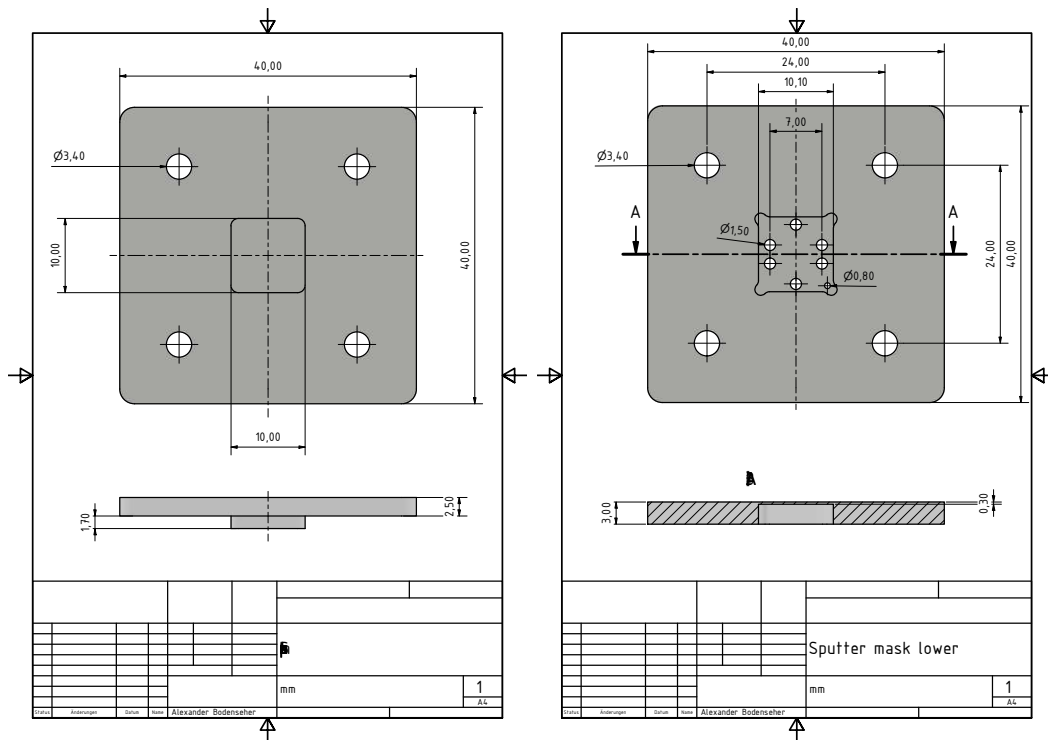
Figure 3.7: Sputter mask made out of FR-2, in which the sample is housed during sputtering. The small hole on the lower right aids in always aligning the sample in the same direction.

Step #	Temperature (°C)	Duration (h)
#1	350	36
#2	383	20
#3	392	12
#4	347	36
#5	407	24
#6	451	24

Table 3.2: Consecutive thermal treatment steps in pure oxygen for IS246. The sample has been sputtered before step #1 and between step #4 and #5.

Step #	Temperature (°C)	Duration (h)
#1	451	24

Table 3.3: Thermal treatment in pure oxygen for IS247. The sample has been sputtered before step #1.

irradiation. A pure oxygen atmosphere was used to prevent oxygen from escaping the YBCO crystal lattice and change as a result T_c.

The thermal treatment steps for samples IS246, IS247, IS248, IS249 are listed in tables 3.2 to 3.5 and the results will be presented and discussed in chapter 4.

3.4 Resistivity and Hall effect measurements

3.4.1 17 T cryostat

The samples have been measured inside the 17 T cryostat. It consists of a double walled evacuated helium reservoir, which contains a composite superconducting magnet, with the outer part of the coil made out of NbTi and the inner made out of Nb_3Sn. The center is occupied by the variable temperature insert (VTI), which is connected to the helium reservoir via a needle valve. A pump creates negative pressure inside the VTI, which draws helium from the reservoir and as

Step #	Temperature (°C)	Duration (h)
#1	362	36
#2	356	1
#3	356	1
#4	218	12
#5	371	12
#6	350	36
#7	407	24
#8	607	24

Table 3.4: Thermal treatment in pure oxygen for IS248. The sample was sputtered before step #1, between steps #1 and #2. The sample did not survive step #8.

Step #	Temperature (°C)	Duration (h)
#1	219	12
#2	368	12
#3	367	12
#4	365	12
#5	224	12
#6	407	24
#7	462	24
#8	608	24

Table 3.5: Thermal treatment in pure oxygen for IS249. The sample was sputtered before step #1 and between steps #6 and #7. The sample did not survive step #8.

a result provides cooling. This is combined with an adjustable resistive heating element, which allows precise adjustment of the temperature inside the VTI.
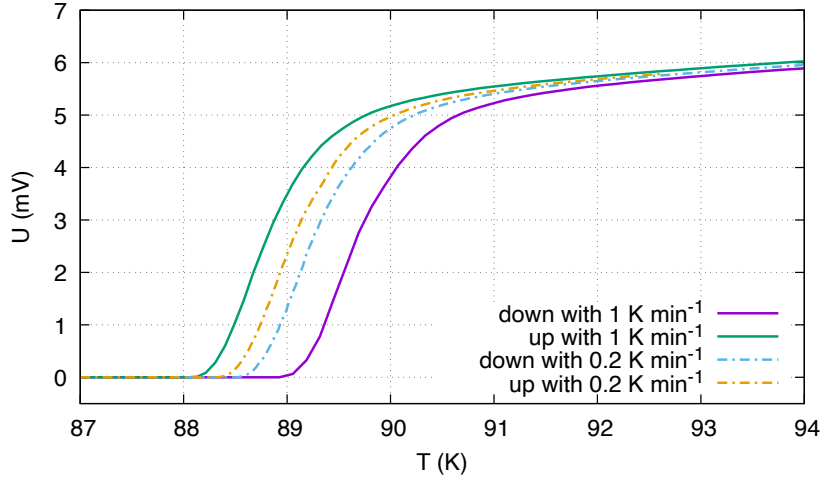

Figure 3.8: Plot comparing the hysteresis while ramping with $1\,\mathrm{K\,min^{-1}}$ and $0.2\,\mathrm{K\,min^{-1}}$

Most measurements where performed by starting above T_c and ramping the temperature down to below T_c. Initially the ramp was set to $1\,\mathrm{K\,min^{-1}}$, but as shown in figure 3.8, it results in a hysteresis larger than $1\,\mathrm{K}$. Therefore, measurements close to T_c have been performed with a ramp of $0.2\,\mathrm{K\,min^{-1}}$. The measurement sequence was modified to change at $150\,\mathrm{K}$ to the slower ramp.

3.4.2 Measurement setup

The sample is inserted into the sample holder (figure 3.11a) for the measurement, and pinned in place by six spring-loaded pins, which are attached to the spring-pin holder (figure 3.12b). The whole stack is attached to the sample rod, which is inserted into the VTI of the $17\,\mathrm{T}$ cryostat.

Two pins (**C** and **D** in figure 3.9) are used for passing current through the
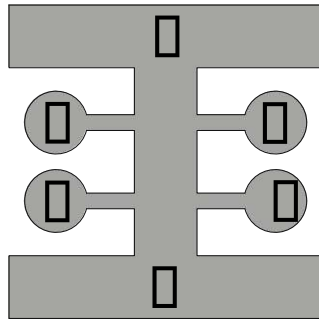
Figure 3.9: Sample layout with named contacts. **C** and **D** are current contacts, **E**, **F**, **H**, **I** are used for measuring voltage.

sample and pins **E**, **F**, **H**, **I** are used for measuring voltage. This setup is called a 4-wire sensing configuration and it has the advantage to eliminate lead resistance from the measurement, since there is no current passing through the voltage sense connections (in this case pins **E**, **F**, **H**, **I**).

There are two relays in the measurement circuit, which are used to switch between resistive measurements (pins **EF**, **HI**) and Hall measurements (pins **EH**, **FI**).

High contact resistance between spring-loaded pins and the samples results in a noisy measurement. Therefore, the resistance between the pins has always been measured after insertion of the sample rod into the VTI. A resistance below $100\,\Omega$ is deemed as acceptable. Higher resistances are caused by degradation of the sputtered silver layer and necessitate etching and resputtering the layer. Short circuits from the current or voltage leads to the $17\,\mathrm{T}$ cryostat are also a concern, and have to be checked.

The current passing through the sample has been set to $10\,\mathrm{mA}$. The chosen setting is always based on trade-offs. A lower current, means lower resistive heating at the interface of sample and pin and therefore a more accurate measurement of the superconducting transition. However, this also means a smaller signal compared to noise. Figure 3.10 shows the same measurement repeated with $1\,\mathrm{mA}$ and $10\,\mathrm{mA}$. The difference between both curves is within

the margin of error, therefore 10 mA has been deemed acceptable.

Since the measured voltages are very low and thermal voltages can be significant, the measurements have been performed in the delta mode. In this mode the precision current supply pulses between ± 10 mA for ten times and the voltmeter cancels out the current independent component of the measurment.
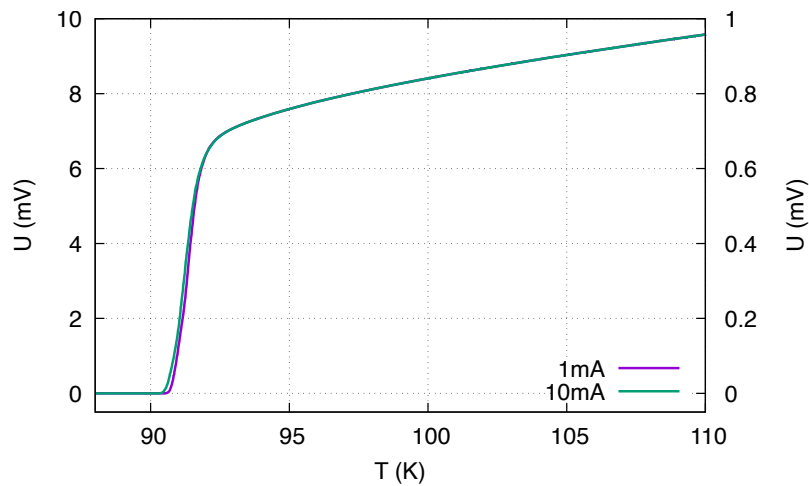

Figure 3.10: Plot comparing the measured voltage based on the current. The axis on the left is for 10 mA, on the right for 1 mA.

3.4.3 T_c evaluation

There are different ways to define and calculate the transition temperature of a superconductor. In this thesis the voltage of the normal state region was extrapolated linearly and intersected with the tangent in the transition region, as illustrated in figure 3.13. This is also called T_c^{onset}.
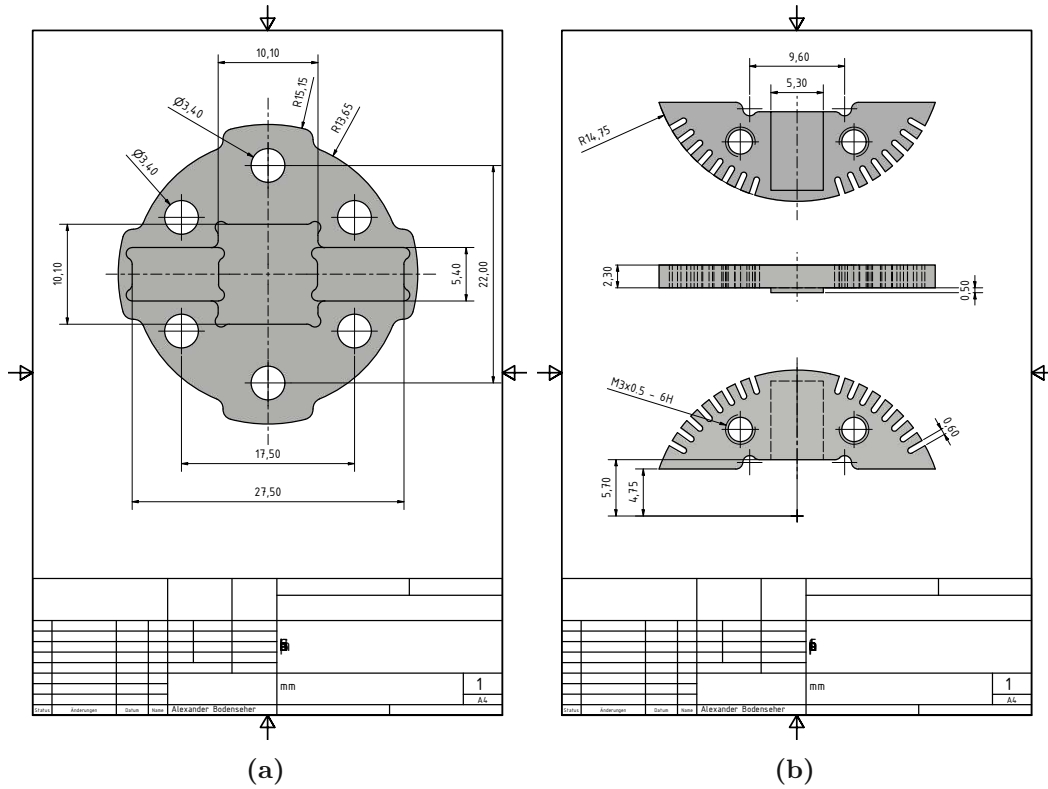
(a)

(b)

Figure 3.11: (a) Sample holder made of FR-2, used for square YBCO on MgO
samples and rectangular coated conductor tapes. (b) Copper contacts
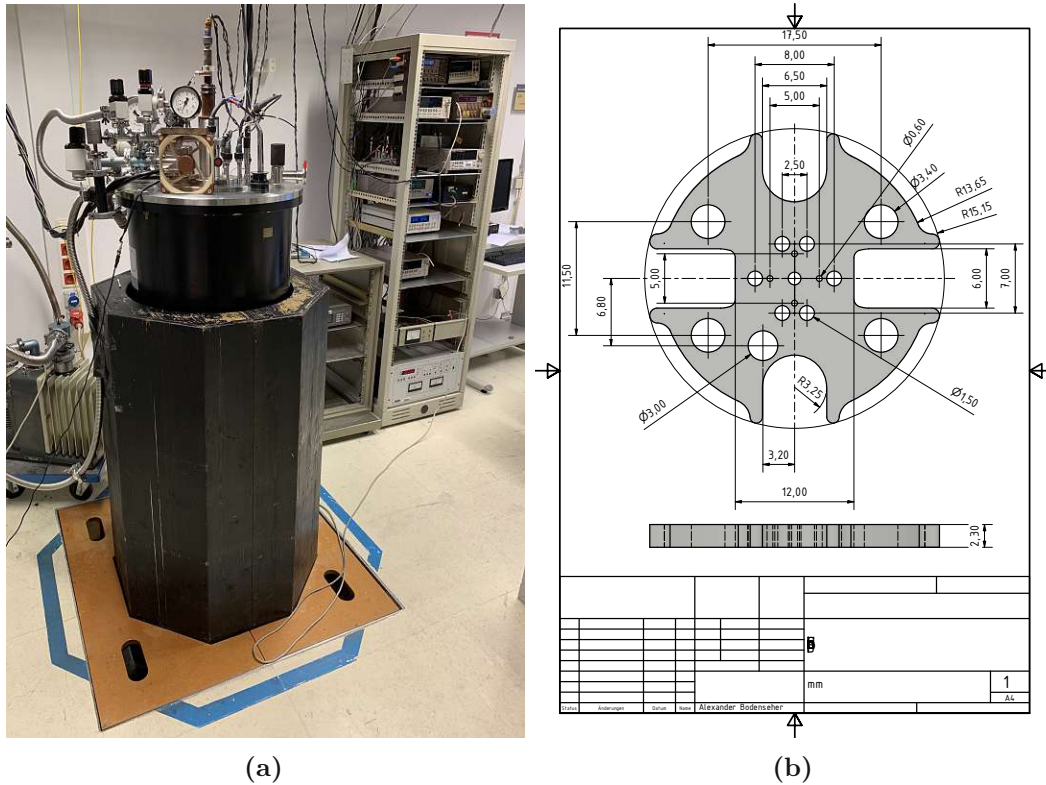with enough clearance for the square samples and spring-loaded pins.

(a) (b)

Figure 3.12: (a) 17 T cryostat. (b) Spring pin holder with 6 1.5 mm holes for providing current and measuring voltage. The 3 mm hole is for inserting the temperature sensor.
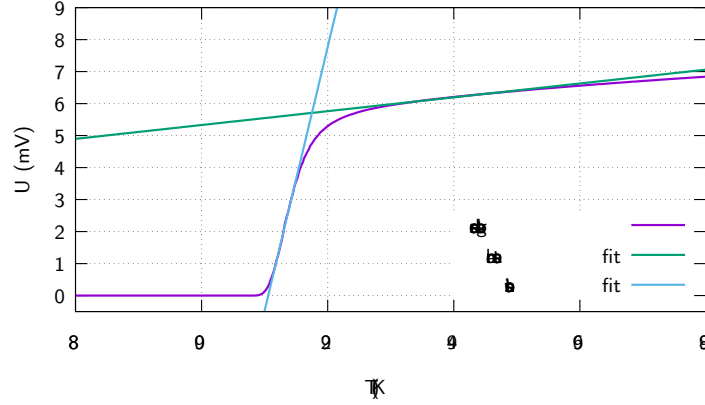
Figure 3.13: Illustration of the T_c evaluation. The measurement was done with IS247 before thermal treatment step #1 and T_c is 91.74 K.

3.4.4 Hall measurements

Electrical charges in an electric and magnetic field experience a Lorentz $\mathbf{F_L} = q(\mathbf{E} + \mathbf{v} \times \mathbf{B})$. In a conductor, this force causes a deviation of the ideal straight path with charge carriers accumulating on one side of the conductor. This imbalance in charge carriers induces an electric field across the conductor, which in turn causes a difference in potential—the Hall voltage U_H.

The Hall voltage can be written as

$$U_\mathrm{H} = R_\mathrm{H}\frac{BI}{t},\tag{3.1}$$

with t being the film thickness and R_H the Hall constant, which is determined by the type of conductor and its charge carriers. For a conductor with holes as charge carriers the Hall constant can be written as:

$$R_\mathrm{H} = \frac{1}{qn_\mathrm{H}},\tag{3.2}$$

thus Hall effect measurements can be used to estimate the charge carrier density

n_{H}.

Hall voltage is measured across contacts **EH**, **FI** as indicated in figure 3.9. Since the spring-loaded pins are not perfectly perpendicular to the current, the measured voltage consists of a resistive and Hall component

$$U_{\mathrm{measured}} = U_{\mathrm{R}} + U_{\mathrm{H}}. \tag{3.3}$$

Equation (3.2) shows, that the sign of the Hall voltage changes with the sign of the magnetic field. Since the current through the sample does not change, the resistive voltage drop remains unchanged. Therefore, it is possible to calculate the Hall voltage component with

$$U_{\mathrm{Hall}} = \frac{1}{2}\left(U_{\mathrm{measured}}^{(+)} - U_{\mathrm{measured}}^{(-)}\right), \tag{3.4}$$

with $U_{\mathrm{measured}}^{(\pm)}$ the measured voltage for positive and negative magnetic field.

4 Results

4.1 Resistive measurements

The results of the resistive measurements of samples IS246, IS247, IS248 and IS249 are presented in figures 4.1 to 4.4. Figure 4.5 shows the development of T_c and the normal state resistivity $5\,\mathrm{K}$ above T_c over the course of the thermal treatment steps.

The resistivity ρ was calculated using

$$\rho = \frac{U}{I}\frac{A}{l}, \tag{4.1}$$

with $I = 10\,\mathrm{mA}$, $l = 2.5\,\mathrm{mm}$, which is the difference between the center of the circular pads as shown in figure 3.1a and $A = 2\,\mathrm{mm} \cdot 1\,\mathrm{\mu m}$.

Defects in the YBCO crystal structure are pair breaking and therefore reduce the superfluid density ρ_s, which is linked to the normal state resistivity and T_c via Homes' law $\sigma_{\mathrm{dc}}T_c \propto \rho_s$. Thermal treatment is expected to reduce the number of defects which in turn increases T_c and reduces the normal state resistivity ρ.

The samples all show a similar unexpected behavior. Before the first thermal treatment step they exhibit a narrow superconducting transition, but after the first step the transition region widens and the normal state resistivity increases (see IS246-(a) $\rightarrow$ IS246-(b), IS247-(a) $\rightarrow$ IS247-(b) and IS248-(a) $\rightarrow$ IS248-(b)).

For IS246 the normal state resistivity remains constant until the 104th hour of thermal treatment, while T_c rises. Afterwards the resistivity and T_c begin to
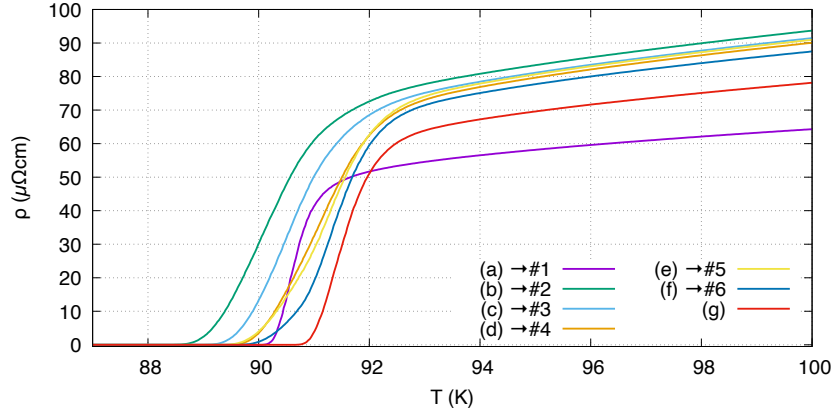
Figure 4.1: Resistive measurements of IS246

decrease with increasing thermal treatment temperature.

Only one thermal treatment step was performed with IS247, which shows the same behavior as IS246 of a widening transition, increasing normal state resistivity and decreasing T_c. One notable result is the increase of the normal state resistivity and decrease of T_c, after sputtering IS247, which contradicts the result presented in section 3.2.1 and the behavior of IS248 and IS249-(f) $\rightarrow$ IS249-(g), which have shown no change in resistivity and T_c.

The normal state resistivity of IS248 remains unchanged after the first thermal treatment step, but T_c decreases and the transition broadens. Afterwards the normal state resistivity and T_c make a jump up and remain constant until the 98$^{\text{th}}$ hour of thermal treatment, where T_c decreases.

There is no measurement of IS249 before the first thermal treatment step, but if there is a pattern, it could be assumed, that IS249-(a) represents the decreased T_c and widened transition. The normal state resistivity and T_c remain constant until the 84$^{\text{th}}$ hours of thermal treatment, after which the normal state resistivity decreases by $\sim$20 %.

The data suggests, that the pristine samples are in an instable condition and the first thermal treatment step changes their properties significantly.
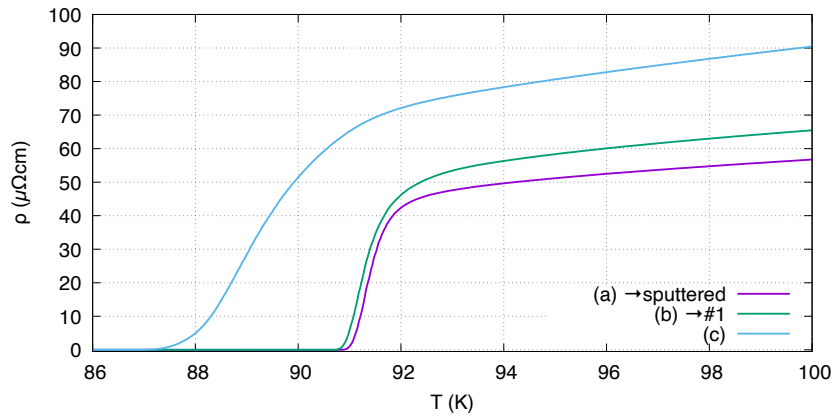
Figure 4.2: Resistive measurements of IS247

Thermally treating them in a temperature between $200\,°C$ to $400\,°C$ stabilizes ρ and T_c. Increasing the temperature above $400\,°C$ causes their properties to change again, with IS246 showing a decrease in T_c and ρ, IS248 a decrease in T_c and IS249 a decrease in ρ.

The last thermal treatment step of IS248 and IS249 were $24\,h$ at $607\,°C$ and $608°$, after which both exhibited a sample resistance in the range of $M\Omega$ and a higher translucency of the YBCO layer. One explanation could be, that the YBCO layer has evaporated off the substrate, but thickness measurements show no change in layer thickness. The cause of this increase in resistivity is still being investigated.

4.2 Hall effect measurements

4.2.1 Hall constant

Hall voltages were measured during temperature sweeps and calculated as described in section 3.4.4. The measurements of IS246 were performed after thermal treatment step #6, for IS248 before step #1 and for IS249 after step
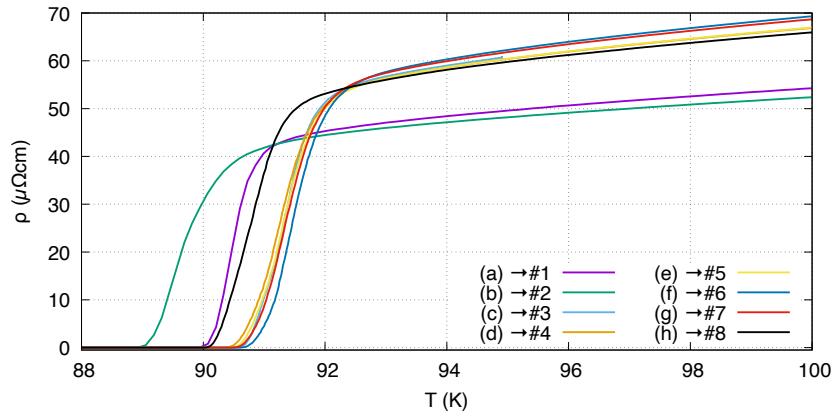
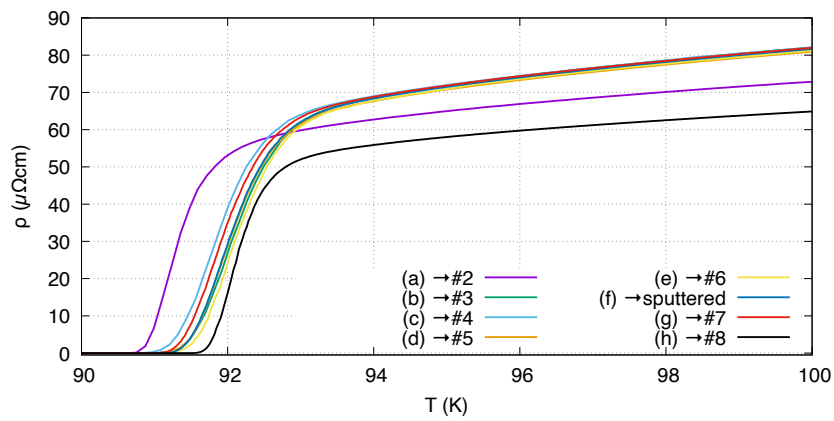**Figure 4.3:** Resistive measurements of IS248

Figure 4.4: Resistive measurements of IS249
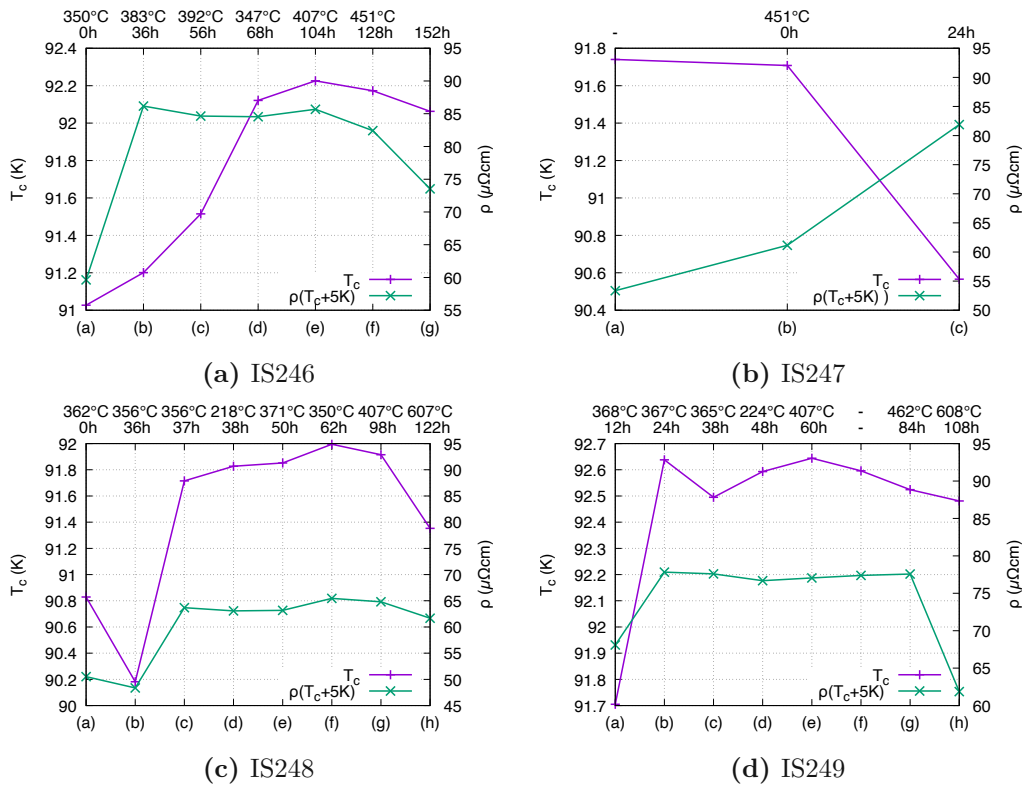
35

Figure 4.5: Development of T_c and $\rho(T_c + 5\,\mathrm{K})$ over consecutive thermal treatment steps. The upper x-axis show the cumulative annealing time and the temperature of the following thermal treatment step.

#1 and before step #2.

Hall voltage were interpolated and plotted with respect to the magnetic field in figure 4.6. Using the expression for the Hall voltage

$$U_{\mathrm{H}} = R_{\mathrm{H}} \frac{BI}{t}, \tag{4.2}$$

with the layer thickness $t = 1 \, \mu\mathrm{m}$ and $I = 10 \, \mathrm{mA}$, the temperature dependent Hall constant can be calculated and is presented in figure 4.7. The shape and order of magnitude of the Hall constant agrees with values reported in [31]. The sudden drop of R_{H} has been reported for optimally doped and slightly underdoped YBCO [32]. Combined with no large changes in T_c (no $T_c < 90 \, \mathrm{K}$) (cf. to reported T_c vs. doping levels in [33]) this indicates, that the thermal treatments steps have not altered the doping state of the samples significantly.

However, the inverse Hall constant of thermally treated IS246 and IS249 is smaller by a factor of one third compared to IS248, which means a decrease in charge carrier density (since the charge carrier density is indirectly proportional to R_H). At the time of measurement IS246 has been thermally treated for a cumulative duration of 152 h and IS249 for only 12 h. The similar shape and quantity of IS246 indicates, that the subsequent thermal treatment steps in the range of 350 °C to 451 °C have not significantly altered the charge carrier density.

4.2.2 Hall angle

It has been shown, that the cotangent of the Hall angle has a quadratic like temperature dependence:

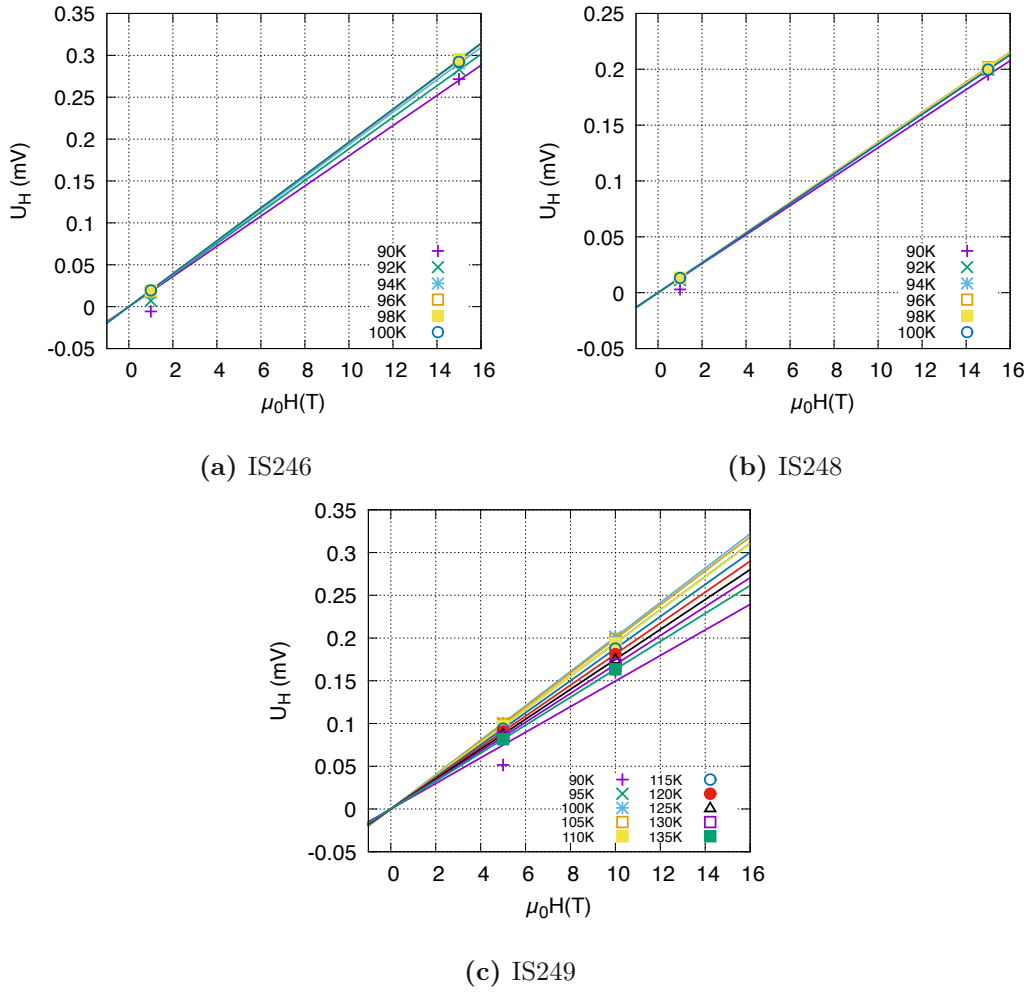$$\cot \theta_{\mathrm{H}} = \frac{\rho_{ab}}{R_{\mathrm{H}} B} = \alpha T^2 + C. \tag{4.3}$$

(a) IS246

(b) IS248

(c) IS249

Figure 4.6: (a) (b) (c) Hall voltage extracted from measurements at different fields. Lines fitted to $U_{\mathrm{H}} = R_{\mathrm{H}}\frac{I}{t}B$
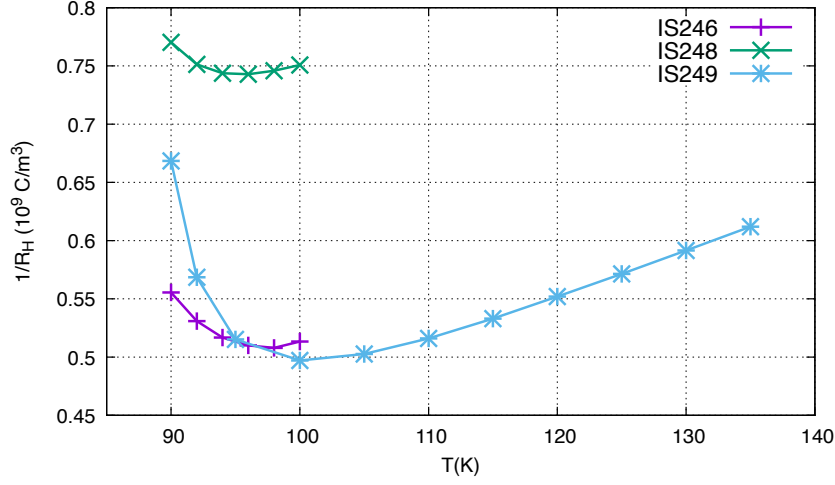
38

Figure 4.7: Temperature dependence of the inverse Hall constant.

Sample	$\alpha(10^{-3}\,\mathrm{K}^{-2})$	β	C
IS249-5T	5	2.06	7.07
IS249-10T	2	2.10	4.70

Table 4.1: Fit parameters for $\cot\theta_{\mathrm{H}} = \alpha T^{\beta} + C$.

Using the resistivity measurement values and the temperature dependent Hall constant, the cotangent of the Hall angle has been plotted in figure 4.8. Since the area below $100\,\mathrm{K}$ is strongly influenced by fluctuations, $\alpha T^{\beta} + C$ has been fitted onto $\cot\theta_{\mathrm{H}}$ for temperatures above $100\,\mathrm{K}$, and the fit parameters are presented in table 4.1. IS249 shows a quadratic behavior. It has been reported, that the slope α of $\cot\theta_{\mathrm{H}}$ is related to the oxygen content of YBCO. [31]. There are however, no step to step measurements of the same sample to investigate this relation.

The Hall angle is defined as the angle between the current density vector and the electric field vector. Therefore, it should increase with larger external magnetic fields. Since the cotangent is monotonically decreasing on the interval $(0, \frac{\pi}{2})$ a higher field results in a smaller $\cot\theta_{\mathrm{H}}$, which can be seen in figure 4.8.
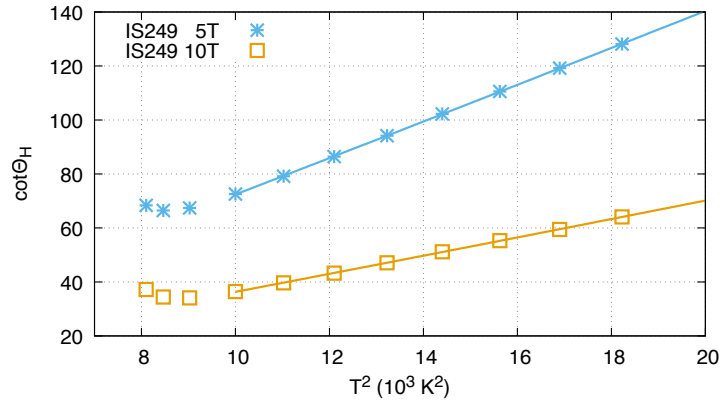
Figure 4.8: $\cot \theta_{\mathrm{H}} = \frac{\rho_{ab}}{R_{\mathrm{H}}B}$ over T^2. Lines fitted to $\alpha T^\beta + C$.

These results, like all Hall effect measurements in this thesis should be taken with a grain of salt, since the Hall constant fit was done using only two points and except for IS249 only in the range of 90 K to 100 K.

5 Conclusions and outlook

In this thesis the preparations for irradiating and measuring bare YBCO films on magnesium oxide samples have been documented. To assess the damage after irradiation and potential improvements after thermal treatment, it is necessary to establish a baseline to which subsequent measurements will be compared.

As of writing of these words samples, IS246 and IS247 are being irradiated inside the central irradiation tube of the TRIGA Mark II research reactor of the Atominstitut and a new batch of samples is being prepared by IFW Dresden.

To summarize, the samples show a similar behavior under thermal treatment. After the first thermal treatment step the superconducting transition region widens and the normal state resistivity increases. It remains fairly constant at annealing temperatures between $350\,°C$ and $400\,°C$ and up to $100\,h$ of consecutive thermal treatment time. Increasing the temperature above $400\,°C$ causes the transition temperature and normal state resistivity to decrease. Temperatures above $600\,°C$ destroy the samples.

Hall effect measurements show an expected decrease of the charge carrier density n_H with decreasing temperature. Thermally treated samples show a reduction in charge carrier density compared to pristine ones, but after the initial thermal treatment step the charge carrier density remains at the same level.

Following is a brief summary of a few key takeaways from this thesis:

- Contacting bare YBCO in a reproducible manner remains challenging.

Sputtering is a good solution, but as discussed in section 4.1 it can change the properties of the sample. The silver layer also degrades over time and new layers have to be sputtered. Sputtering is still a better solution than conductive silver paint and much cheaper than gold physical vapor deposition.
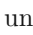
- Complementary ways to evaluate the doping state of the samples would be of interest. In this thesis the inverse of the temperature dependent Hall constant was used, but there are more methods available. A technique to differentiate between over-, under- and optimally doped is presented in [5], but it requires temperature sweeps up to almost ambient temperature. Also, [31] suggests, that the slope α of the cotangent of the Hall angle is related to the doping level δ.

- The results of the Hall effect are interesting and confirm results from literature, but to calculate the Hall constant reliably more Hall effect measurements over a wider field and temperature range are needed.

- Last but not least, the measurement data of the irradiated samples is the actual information of interest for this thesis and its interpretation in the context of [1].

This thesis is merely a snapshot on ongoing research conducted by the author and his collaborators, with the most exciting results still to be discovered.

References

[1] R. Unterrainer, D. X. Fischer, A. Lorenz, and M. Eisterer, „Recovering the perfor-mance of irradiated high-temperature superconductors for use in fusion magnets“, *Superconductor Science and Technology*, vol. 35, no. 4, 04LT01, Feb. 2022. DOI: https://doi.org/10.1088/1361-6668/ac4636.

[2] D. X. Fischer, „Effect of neutron radiation damage on coated conductors for fusion magnets“, en, Ph.D. dissertation, Technische Universität Wien, 2019. DOI: 10.34726/HSS.2019.27911.

[3] M. Tinkham, *Introduction to superconductivity*. Mineola, N.Y: Dover Publications, 2004, ISBN: 9780486435039.

[4] R. Gross and A. Marx, *Festkörperphysik*, ger. Berlin: De Gruyter, 2018, ISBN: 978-3-11-055822-7.

[5] A. Stangl, „Oxygen kinetics and charge doping for high critical current YBCO films“, Licensed under ⊚①⑤⊝, Ph.D. dissertation, Universitat Autònoma de Barcelona, Barcelona, 2019, ISBN: 9788449087103.

[6] H. K. Onnes, „The Superconductivity of Mercury“, *Comm. Phys. Lab. Univ. Leiden*, vol. 122, pp. 122–124, 1911.

[7] W. Meißner and R. Ochsenfeld, „Ein neuer Effekt bei Eintritt der Supraleitfähigkeit“, *Die Naturwissenschaften*, vol. 21, no. 44, pp. 787–788, Nov. 1933. DOI: 10.1007/bf01504252.

[8] F. London and H. London, „The electromagnetic equations of the supraconductor“, *Proceedings of the Royal Society of London. Series A - Mathematical and Physical Sciences*, vol. 149, no. 866, pp. 71–88, Mar. 1935. DOI: https://doi.org/10.1098/rspa.1935.0048.

[9] A. B. Pippard and W. L. Bragg, „An experimental and theoretical study of the relation between magnetic field and current in a superconductor“, *Proceedings of the Royal Society of London. Series A. Mathematical and Physical Sciences*, vol. 216, no. 1127, pp. 547–568, Feb. 1953. DOI: 10.1098/rspa.1953.0040. [Online]. Available: https://royalsocietypublishing.org/doi/10.1098/rspa.1953.0040.

[10] L. P. Gor'kov, „Microscopic derivation of the Ginzburg–Landau equations in the theory of superconductivity“, *Journal of Experimental and Theoretical Physics*, vol. 36, pp. 1364–1367, Jan. 1959.

[11] A. A. Abrikosov, „On the Magnetic properties of superconductors of the second group", *Journal of Experimental and Theoretical Physics*, vol. 5, pp. 1174–1182, 1957.

[12] F. Bouquet and J. Bobroff, *Superconductor interactions with magnetic field*, Licensed under ⓒⒾⓄ 4.0, Nov. 2011. [Online]. Available: https://commons.wikimedia.org/wiki/File:Superconductor_interactions_with_magnetic_field.png.

[13] L. N. Cooper, „Bound Electron Pairs in a Degenerate Fermi Gas", *Physical Review*, vol. 104, no. 4, pp. 1189–1190, Nov. 1956. DOI: 10.1103/physrev.104.1189.

[14] J. Bardeen, L. N. Cooper, and J. R. Schrieffer, „Microscopic Theory of Superconductivity", *Physical Review*, vol. 106, no. 1, pp. 162–164, Apr. 1957. DOI: 10.1103/physrev.106.162.

[15] J. Bardeen, L. N. Cooper, and J. R. Schrieffer, „Theory of Superconductivity", *Physical Review*, vol. 108, no. 5, pp. 1175–1204, Dec. 1957. DOI: 10.1103/physrev.108.1175.

[16] J. G. Bednorz and K. A. Müller, „Possible high T_c superconductivity in the Ba-La-Cu-O system", *Zeitschrift für Physik B Condensed Matter*, vol. 64, no. 2, pp. 189–193, Jun. 1986. DOI: 10.1007/bf01303701.

[17] M. K. Wu *et al.*, „Superconductivity at 93 K in a new mixed-phase Y-Ba-Cu-O compound system at ambient pressure", *Physical Review Letters*, vol. 58, no. 9, pp. 908–910, Mar. 1987. DOI: https://doi.org/10.1103/PhysRevLett.58.908.

[18] A. Damascelli, Z. Hussain, and Z.-X. Shen, „Angle-resolved photoemission studies of the cuprate superconductors", *Reviews of Modern Physics*, vol. 75, no. 2, pp. 473–541, Apr. 2003. DOI: 10.1103/revmodphys.75.473.

[19] M. Buchanan, „Mind the pseudogap", *Nature*, vol. 409, no. 6816, pp. 8–11, Jan. 2001. DOI: 10.1038/35051238.

[20] J. Zaanen, „Why the temperature is high", *Nature*, vol. 430, no. 6999, pp. 512–513, Jul. 2004. DOI: https://doi.org/10.1038/430512a.

[21] Y. J. Uemura *et al.*, „Universal Correlations between T_c and $\frac{n_s}{m^*}$ (Carrier Density over Effective mass) in high-T_c Cuprate Superconductors", *Physical Review Letters*, vol. 62, no. 19, pp. 2317–2320, May 1989. DOI: 10.1103/physrevlett.62.2317.

[22] I. Božović, X. He, J. Wu, and A. T. Bollinger, „Dependence of the critical temperature in overdoped copper oxides on superfluid density", *Nature*, vol. 536, no. 7616, pp. 309–311, Aug. 2016. DOI: 10.1038/nature19061.

[23] C. C. Homes *et al.*, „A universal scaling relation in high-temperature superconductors", *Nature*, vol. 430, no. 6999, pp. 539–541, May 2004. DOI: 10.1038/nature02673.

[24] S. T. Hartman *et al.*, „Direct observation of apical oxygen vacancies in the high-temperature superconductor $YBa_2Cu_3O_{7-x}$", *Physical Review Materials*, vol. 3, no. 11, p. 114 806, Nov. 2019. DOI: 10.1103/PhysRevMaterials.3.114806.

[25] Rhelmich, *YBCO structure*, Licensed under ⓒⒾⓄ 3.0, Oct. 2006. [Online]. Available: https://commons.wikimedia.org/wiki/File:YBCO_structure.jpg.

[26] D. A. Brown *et al.*, „ENDF/B-VIII.0: The 8th Major Release of the Nuclear Reaction Data Library with CIELO-project Cross Sections, New Standards and Thermal Scattering Data", *Nuclear Data Sheets*, vol. 148, pp. 1–142, Feb. 2018. DOI: `10.1016/j.nds.2018.02.001`. [Online]. Available: `https://www-nds.iaea.org/exfor/endf.htm`.

[27] R. Fuger, F. Hengstberger, M. Eisterer, and H. W. Weber, „Scan Techniques for Coated Conductors", *IEEE Transactions on Applied Superconductivity*, vol. 17, no. 2, pp. 3753–3756, Jun. 2007. DOI: `10.1109/tasc.2007.899646`.

[28] M. Lao, „Current limiting mechanism in coated conductors", eng, Ph.D. dissertation, Technische Universität Wien, Wien, 2017. [Online]. Available: `https://catalogplus.tuwien.at/permalink/f/8j3js/UTW_alma2165938780003336`.

[29] Y. Suzuki, T. Kusaka, A. Aoki, T. Aoyama, T. Yotsuya, and S. Ogawa, „The Contact Resistance of the $YBa_2Cu_3O_{7-\delta}$-Metal Film System", *Japanese Journal of Applied Physics*, vol. 28, no. Part 1, No. 12, pp. 2463–2467, Dec. 1989. DOI: `10.1143/jjap.28.2463`.

[30] T. Baumgartner, „Transport current anisotropy in melt-textured high-temperature superconductors", eng, M.S. thesis, Vienna University of Technology, Vienna, 2009. [Online]. Available: `https://catalogplus.tuwien.at/permalink/f/8j3js/UTW_alma2141947670003336`.

[31] B. Wuyts, E. Osquiguil, M. Maenhoudt, S. Libbrecht, Z. X. Gao, and Y. Bruynseraede, „Influence of the oxygen content on the normal-state Hall angle in $YBa_2Cu_3O_{x_n}$ films", *Physical Review B*, vol. 47, no. 9, pp. 5512–5515, Mar. 1993. DOI: `10.1103/physrevb.47.5512`.

[32] K. Segawa and Y. Ando, „Intrinsic Hall response of the CuO planes in a chain-plane composite system of $Y_1Ba_2Cu_3O_y$", *Physical Review B*, vol. 69, no. 10, p. 104 521, Mar. 2004. DOI: `10.1103/physrevb.69.104521`. [Online]. Available: `https://journals.aps.org/prb/abstract/10.1103/PhysRevB.69.104521`.

[33] Z. Mori, T. Doi, and Y. Hakuraku, „Oxygen diffusion in c-axis oriented $YBa_2Cu_3O_{7-\delta}$ thin films", *Journal of Applied Physics*, vol. 110, no. 3, p. 033 915, Aug. 2011. DOI: `10.1063/1.3619861`. [Online]. Available: `https://aip.scitation.org/doi/10.1063/1.3619861`.